



Phase transition of TiO₂ nanoparticles into titanate nanorods via hydrothermal reactions

Diego Morais da Silva^{1,2} · Beatriz Rossi Canuto de Menezes¹ · Vinicius Danilo Nonato Bezzon³ · Thais Larissa do Amaral Montanheiro¹ · Erenilda Ferreira de Macedo⁴ · Dayane Batista Tada⁴ · Gilberto Petraconi¹ · Gilmar Patrocínio Thim¹

© Springer Nature Switzerland AG 2019

Abstract

Titanate nanorod synthesis method is extremely important due to their large application in electronic, catalysis, and biological areas. However, works reporting the influence of synthesis parameters on the structure, morphology, and properties of titanate nanorods are still rare. Therefore, this work aims to analyze the preparation of titanate nanorods from TiO₂ nanoparticles via hydrothermal reaction. The microstructure and morphological properties were evaluated as a function of time, temperature and precursor nature (anatase or anatase/rutile mixture) by X-ray powder diffraction, Raman spectroscopy, transmission electron microscopy and field-emission scanning electron microscopy. The crystallinity of the precursor was the main parameter for the titanate nanorods formation. Besides, temperature has also a direct influence in the fibril morphology. The use of low temperature and anatase/rutile mixture was not able to produce titanate nanorods. Only the use of higher temperatures and pure anatase resulted in rod-like titanates, which showed higher methylene blue photodegradation efficiency than TiO₂ nanoparticles.

Keywords TiO₂ nanoparticles · Titanate nanorods · Hydrothermal reaction · Phase transition · Photodegradation

1 Introduction

Manny efforts have been invested in the development of nanometer scale materials to improve their performance and, consequently, expand their applications. Titanium dioxide (TiO₂) is a semiconductor with three different crystal structures: anatase, rutile, and brookite. Rutile is the most stable form of TiO₂ under ambient conditions. However, anatase phase becomes more stable in nanometer size (under 15 nm) [1]. TiO₂ is often used in solar cells [2–4], gas-sensors [5], cosmetics [6], antimicrobial agents [7], food additives [8], textiles [9], paints [10], aerogels [11], and scaffolds for tissue regeneration [12]. The great

number of TiO₂ applications are due to the TiO₂ unique properties, such as biocompatibility, chemical stability, low cost, photocatalytic activity [13], and a wide-bandgap semiconductor (approximately 3.3 eV) [14]. Studies related to TiO₂ synthesis routes are extremely necessary, especially for production of nanometer-sized particles, due to the increasing demand of TiO₂-based materials. The intrinsic relation of particle size with physical and chemical properties broaden the use of TiO₂ in nanometric scale. In this way, optimizing the synthesis process to obtain TiO₂ in nanometric scale with better structural quality, repeatability, reproducibility and with appropriate yield is required.

✉ Diego Morais da Silva, dmoraidsm@gmail.com | ¹Laboratório de Plasmas e Processos, Instituto Tecnológico de Aeronáutica (ITA), Praça Marechal Eduardo Gomes, 50, Vila das Acácias, São José dos Campos, SP 12228-970, Brazil. ²Instituto Federal de Educação, Ciência e Tecnologia do São Paulo (IFSP), Rodovia Presidente Dutra, Km 145, Jardim Diamante, São José dos Campos, SP, Brazil. ³Centro de Ciências Naturais e Humanas, Universidade Federal do ABC, Avenida dos Estados, 5001, Santa Teresinha, Santo André, SP 09210580, Brazil. ⁴Laboratório de Nanomateriais e Nanotoxicologia, Instituto de Ciência e Tecnologia, Universidade Federal de São Paulo, Rua Talim, 330, Jardim Aeroporto, São José dos Campos, SP 12231280, Brazil.



SN Applied Sciences (2019) 1:945 | <https://doi.org/10.1007/s42452-019-1004-4>

Received: 15 May 2019 / Accepted: 28 July 2019 / Published online: 31 July 2019

Nanoparticles of TiO_2 can be synthesized using several techniques, including sol–gel, electrochemistry, and hydrothermal method [15]. In the hydrothermal method, an aqueous solution is submitted to pressure and temperature, using an autoclave. In this technique, the structure, morphology, and properties of the products will be determined by the solution volume and reaction temperature. The hydrothermal method is extensively used to obtain anatase structure, but also can be used to obtain titanate in tubular and fibrillar morphologies from TiO_2 nanoparticles. The reagents, temperature and pressure will define the final structures and morphologies of tubular titanates [16].

During the hydrothermal process, TiO_2 nanoparticles reacts with concentrated sodium hydroxide or diluted acid solution, disrupting their structures. The recrystallization will occur by the formation of titanate sheets. Due to the hydrogen deficiency on the surface of the titanate sheets, the layers fold themselves, forming the nanorods. Reactive groups on the surfaces of titanate sheets are eliminated when the surface tension is reduced, resulting in an arrangement with less surface energy and more stable structures [17]. Therefore, the formation of titanate nanorods occur after the recrystallization as titanate sheets, followed by their rolling [18].

Titanate nanorods show great relevance due to their elevated surface area [19], ability to influence cellular response [20], high refractive index [21], catalytic activity, and strong metal support interaction [22]. Also, the higher number of reactive groups, such as hydroxyl, on titanate nanorod surfaces facilitates the surface modification, increasing their range of application [23]. Titanate nanorods have several applications, including photovoltaic cells, batteries [24], polymer nanocomposites [25], supercapacitors [26], dental cements [21], implant surfaces [27], catalysts, sensors, fuel cells, and energy storage devices [22].

The study of synthesis methods of TiO_2 nanoparticles and titanate nanorods are extremely important due to their vast number of applications. Understanding the synthesis routes will allow the preparation of materials with better structures and properties, adapting them to their applications. In this work, different conditions (time and temperatures) of hydrothermal synthesis of titanate nanorods were studied. Two different precursors with different crystalline phases were used as titanate nanorod precursors, allowing to verify how the presence of anatase or rutile nanocrystals influence the morphology of the titanate nanorod. According to the results, the precursor phase and temperature of hydrothermal synthesis were the most important parameters in the preparations of titanate nanorods. Photodegradation tests showed that photodegradation efficiency is higher for titanates

nanorods when compared to TiO_2 nanoparticles. Notably, the photodegradation efficiency increased with the titanate nanorod content in each sample.

2 Methodology

2.1 Synthesis of TiO_2 nanoparticles

TiO_2 nanoparticles were synthesized using hydrothermal method. Initially, 0.18 g of sodium dodecyl sulfate (Synth, 90%) was dissolved into 3 mL of deionized water at ambient temperature. After complete dissolution, 40 mL of ethanol (Neon, 99.8%) and 2.5 mL of acetic acid (Synth, 99.7%) were added to the mixture and maintained under stirring until complete homogenization. Then, 5 mL of titanium (IV) isopropoxide (Sigma-Aldrich, 97%) was added to the reaction vessel, stirring for 20 min. Finally, the mixture was transferred to a Teflon-lined stainless autoclave to carry out the hydrothermal treatment at 160 °C for 8 h. The resulting powder was centrifuged and thoroughly washed with water. Finally, the sample was dried at 80 °C for 24 h and calcinated at 600 °C for 1 h. The hydrothermal synthesized TiO_2 was labeled H- TiO_2 .

2.2 Synthesis of titanate nanorods

TiO_2 nanorods were also synthesized using hydrothermal method, following the procedure of Kasuga et al. (1998) [28]. Two different TiO_2 nanoparticles were used as precursors: (1) the hydrothermal synthesized TiO_2 (H- TiO_2) and (2) commercial TiO_2 (Aeroxide® P25, Evonik, 99.5%) denoted as C- TiO_2 . About 0.5 g of TiO_2 nanoparticles was dispersed in sodium hydroxide (NaOH, Synth, 98%) aqueous solution (10 mol L⁻¹) and transferred to a Teflon-lined stainless autoclave. The autoclave was heated at two different temperatures (100 and 150 °C) and two different times (24 and 48 h). The resulting powder was centrifuged and thoroughly washed with water until reach the neutral pH. Then, the material was washed with hydrochloric acid (HCl, Neon, 37%) aqueous solution (0.1 mol L⁻¹) until reach pH 4 and subsequently, washed with deionized water to remove excess of chlorides. Finally, the sample was dried at 80 °C for 24 h. Figure 1 presents a diagram of the synthesis parameters used in the production of titanate nanorods, where HNF and CNF refers to TiO_2 nanorods obtained from H- TiO_2 and C- TiO_2 , respectively.

2.3 Microstructural characterization of TiO_2 nanoparticles and titanate nanorods

Both TiO_2 nanoparticles and titanate nanorods were characterized by X-ray powder diffraction (XRD). XRD analysis

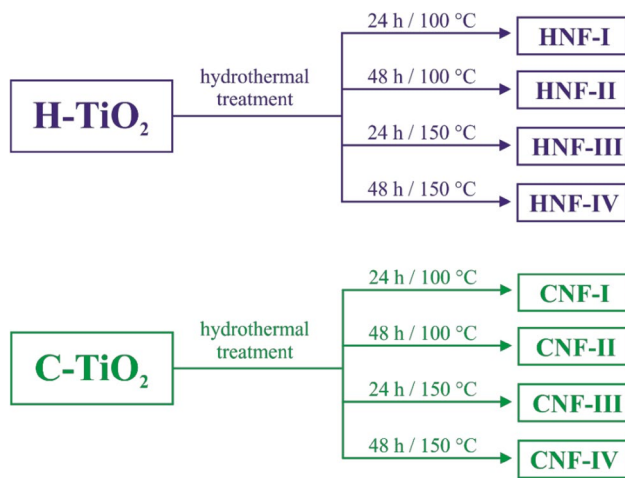


Fig. 1 Synthesis parameters used in the production of titanate nanorods

were performed using a PANalytical Philips X'Pert with CuK α radiation ($\lambda = 1.5406 \text{ \AA}$) in the 2θ range of 10° – 100° at a scan speed rate of $1^\circ/\text{min}$ and step size of 0.02° . Rietveld [29] refinements were performed using the TOPAS Academic V5 [30]. Raman spectroscopy measurements were carried out for TiO_2 nanoparticles and titanate nanorods using a Horiba LabRam HR Evolution, operating at 532 nm. The spectra were measured in the 50 – 800 cm^{-1} range. The morphology of TiO_2 nanoparticles were examined by transmission electron microscopy (TEM) FEI TECNAI G² at 200 kV. Size distributions were determined from TEM pictures by measuring the size of 10 particles using image analysis software Image J. Titanate nanorod morphologies were analyzed by Field-emission scanning electron microscopy (FE-SEM) Jeol JSM-5310 operated at 30 kV.

2.4 Photodegradation

The methylene blue (MB) photodegradation by each sample from HNF group and H- TiO_2 was evaluated by preparing nanoparticles suspension in type I water at the concentration of 0.6 mg/mL . Then, $156 \text{ }\mu\text{L}$ of an aqueous solution of MB (0.385 mM) were added to 4 mL of each nanoparticle suspension. Therefore, the MB concentration in the mixture was of $15 \text{ }\mu\text{M}$. The nanoparticles suspensions with MB were stirred in the dark by using a tube agitator (home produced by robotic group of UNIFESP-Forgers) for 2 h in order to promote MB adsorption on nanoparticles. The UV–Vis spectra (FS5, Edinburgh Instruments) of each sample were measured after stirring (t_0) and after 30 min (t_{30}) under UV irradiation (365 nm ; 36 W). Samples of each type of nanoparticle without MB were also irradiated in order to evaluate the photo stability of the nanoparticles. A solution of

MB was also irradiated in the absence of nanoparticles in order to confirm that the photodegradation was due to the activity of nanoparticles and not only due to irradiation. In addition, samples of HNF-III were irradiated for 60 and 120 min. Since the photodegradation of MB by HNF-IV was too fast, the assay was repeated by using these nanoparticles and a higher concentration of MB ($30 \text{ }\mu\text{M}$). The UV–Vis spectra of the samples were measured after 5, 10, 20 and 30 min of UV irradiation. The efficiency of photodegradation was calculated by using the following equation:

$$E_p = \left(1 - \frac{C}{C_0}\right) * 100$$

where C_0 is the initial concentration of MB at time t_0 and C is the concentration of MB after the irradiation under UV light. The absorbance signal due to light scattering of all nanoparticles was subtracted from the absorbance value of MB by measuring UV–Vis spectra of nanoparticles suspension without MB.

3 Results and discussion

3.1 Microstructural characterization of TiO_2 nanoparticles

Figure 2 shows TEM micrographs of samples C- TiO_2 and H- TiO_2 . The average particle size was estimated from TEM micrographs as $\sim 20 \pm 3 \text{ nm}$ for C- TiO_2 and $\sim 10 \pm 1 \text{ nm}$ for H- TiO_2 . Several techniques can be used to produce TiO_2 nanoparticles, resulting in different crystallographic structure and properties. The C- TiO_2 particles here used were produced by vapor-fed flame pyrolysis in an industrial process [31]. In this case, the synthesis parameters are optimized to produce the highest amount of material. On the other hand, hydrothermal method here used is a known a process to obtain small particles without great concerns about the production yield [14]. Despite of the correct morphology of each particle is difficult to define using TEM, since the particles are shown as simple projection [32], one can conclude that C- TiO_2 and H- TiO_2 presented irregular shape, similar to distorted squares, rectangles, and circles [31]. Both samples appear to be highly crystalline and no remarkable difference in the particle shapes can be observed.

Figure 3 shows XRD patterns of samples C- TiO_2 and H- TiO_2 . Both samples exhibit similar peaks in the XRD patterns, which can be indexed to the tetragonal phase (space group $I4_1/amd$) of anatase, identified mainly by the peak with higher intensity at (101) plane (JCPDS

Fig. 2 TEM micrograph of **a** sample C-TiO₂ and **b** sample H-TiO₂

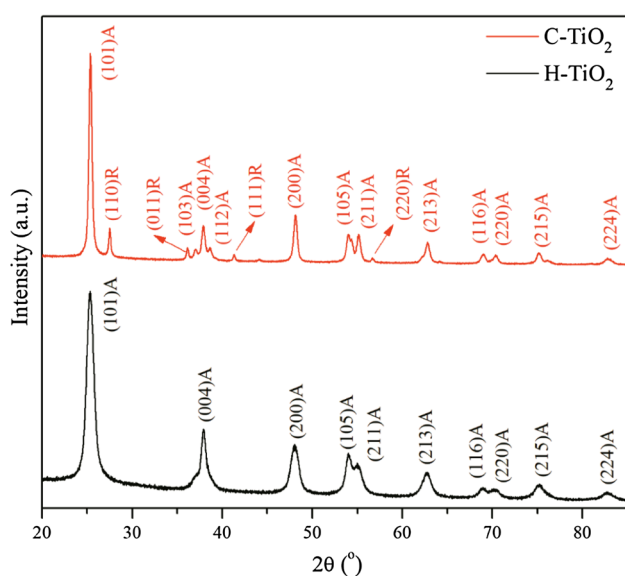
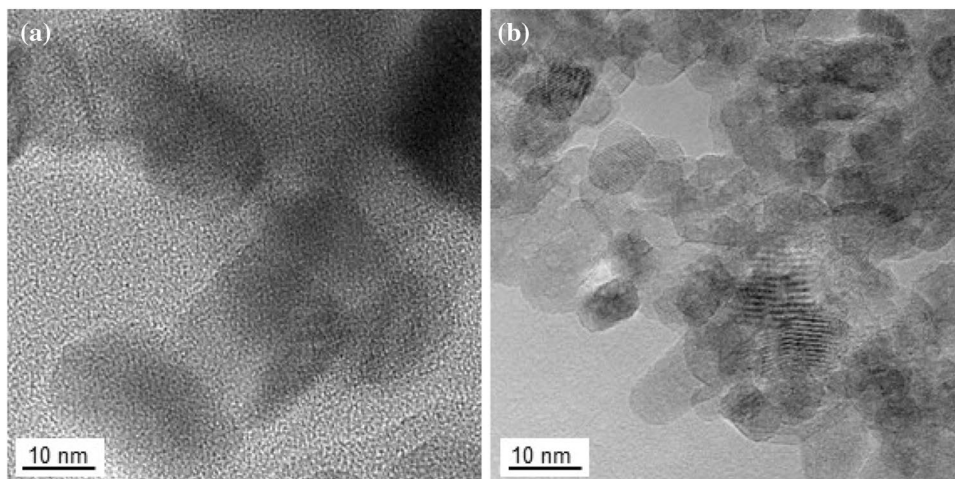


Fig. 3 XRD patterns of samples C-TiO₂ and H-TiO₂ (Letter “A” refers to anatase phase and “R” refers to rutile)

21-1272) [33]. For C-TiO₂ sample, less intense peaks of tetragonal rutile phase at (110), (011), (111), and (220) were also observed (JCPDS 21-1276) [34].

The Rietveld refinements and the quantitative phase analysis of C-TiO₂ and H-TiO₂ samples were performed to achieve the lattice parameters, weight fraction for each phase and the average crystallite size. The Crystallographic Information Files (CIFs) used for the refinements were obtained at the ICSD database, under the code 172914 (Anatase) and 257864 (Rutile). The Rietveld plots and structural results are shown in Fig. 4 and Table 1, respectively. The agreement factors (R_{wp} , R_{Bragg} and GOF) indicated a good agreement between calculated and observed diffractograms.

The lattice parameters obtained by Rietveld refinement is in good agreement with those published in the literature, as showed in Table 1. A fraction of 15.6 wt% of rutile phase was observed in sample C-TiO₂. According to Bickley et al. [32] the rutile phase can be present as individual particles or mixed with the anatase phase, producing heterojunction structures. This mixed material can be found as rutile clusters mixture to anatase nanoparticles or thin layer of rutile covering the anatase nanoparticles [31, 32]. For the hydrothermal TiO₂ sample, only anatase phase was observed, indicating high phase purity. This result agrees with literature that showed the presence of rutile in sample C-TiO₂.

The average crystallite size was calculated during the Rietveld refinement routine and compared with particles size measured by TEM images and are presented in Table 2. Rietveld refinement provides crystallite sizes for each phase. So, for the sample C-TiO₂, two crystallite sizes are observed, one for anatase and one for rutile. On the other hand, particles sizes measured by TEM does not take into account the different phases. The results showed that the particles sizes obtained by TEM are similar to the average crystallite sizes calculated using Rietveld refinement.

Figure 5 presents the Raman spectra of sample H-TiO₂ and sample C-TiO₂. The sample H-TiO₂ showed Raman bands at around 150, 200, 400, 518, and 641 cm⁻¹, which can be assigned to E_g, E_g, B_{1g}, A_{1g}, and E_g modes of tetragonal anatase phase, respectively. The sample C-TiO₂ presented bands related to anatase phase, but also showed a weak band at around 450 cm⁻¹ (Fig. 4b), corresponding to E_g mode of rutile phase [35]. This result is in agreement with XRD results, confirming the presence of rutile in C-TiO₂.

The Raman spectra also gives information about the crystallinity and the microstructure of the studied materials [35]. In order to give a clearly understanding about the difference between the C-TiO₂ and H-TiO₂ samples, the

Fig. 4 Rietveld refinements plots of **a** sample C-TiO₂ and **b** sample H-TiO₂

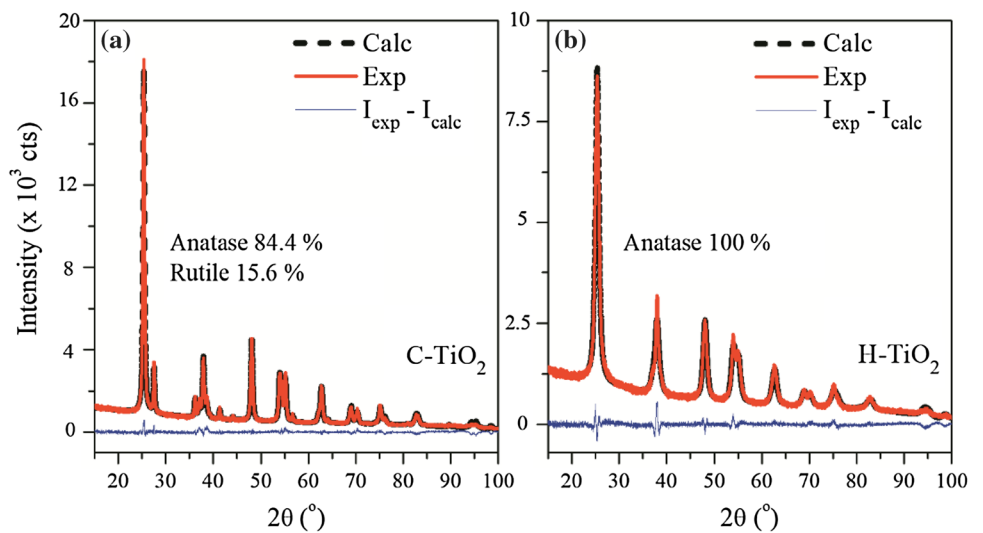


Table 1 Results obtained from Rietveld refinements of sample C-TiO₂ and sample H-TiO₂ powders. Letter “A” refers to anatase phase and “R” to rutile phase

Sample	Phases	a (Å)	a* (Å)	c (Å)	c* (Å)	R _{wp} (%)	R _{Bragg} (%)	GOF
C-TiO ₂	(A)	3.7852	3.78465	9.5066	9.5123	6.3	2.4	1.8
	(R)	4.5936	4.6012	2.9569	2.9637	6.3	3.1	1.8
H-TiO ₂	(A)	3.7899	3.78465	9.4971	9.5123	5.7	1.1	1.7

a*, c* = theoretical lattice parameters from CIF files

Table 2 Average crystallite size (nm) calculated from Rietveld refinement and particle size (nm) measured in TEM images

Samples	Phase	Rietveld refinement (nm)	TEM images (nm)
C-TiO ₂	(A)	21.4 ± 0.2	20 ± 3
	(R)	33 ± 2	
H-TiO ₂	(A)	9.0 ± 0.1	10 ± 1

full-widths at half-maximum (FWHM) and Raman shift of anatase most intense bands are given in Table 3.

C-TiO₂ sample presented a decrease in the Raman shift and the FWHM, indicating that its crystallite size is larger when compared to sample H-TiO₂ [35], as it was already verified by TEM and XRD. The variations in Raman spectra between H-TiO₂ and C-TiO₂ can also be related to the presence of rutile phase in addition to anatase one [36] in the

Fig. 5 Raman spectra of sample H-TiO₂ and sample C-TiO₂; **a** full curves and **b** curve on the region between 300 and 800 cm⁻¹

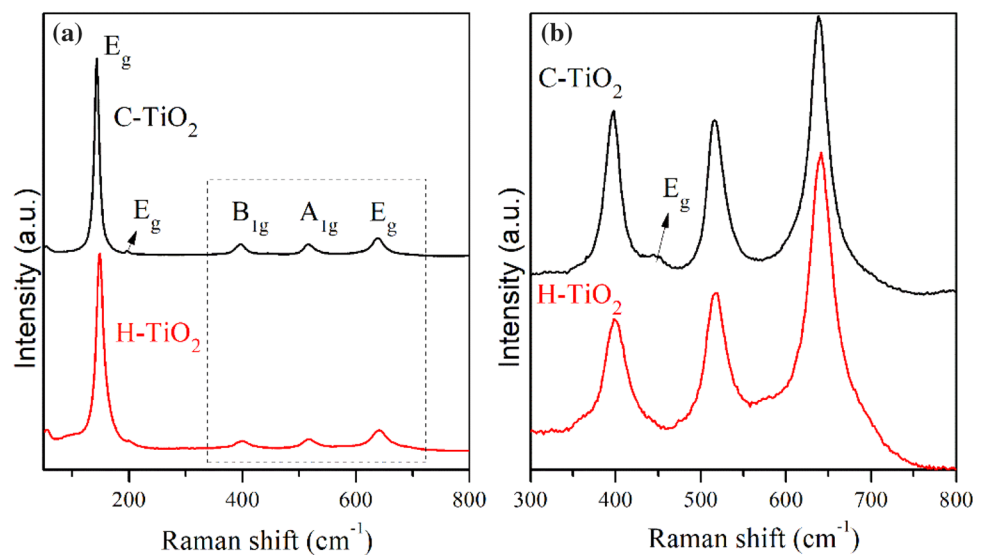


Table 3 The FWHM and Raman shift of anatase phase from sample H-TiO₂ and sample C-TiO₂

Sample	E _g		B _{1g}		A _{1g}		E _g	
	Shift (cm ⁻¹)	FWHM	Shift (cm ⁻¹)	FWHM	Shift (cm ⁻¹)	FWHM	Shift (cm ⁻¹)	FWHM
H-TiO ₂	149	22	400	27	518	29	641	37
C-TiO ₂	143	13	397	24	518	25	638	30

sample C-TiO₂. Raman results are in good agreement with TEM and XRD analysis.

3.2 Microstructural characterization of TiO₂ nanorods

Figure 6a-d shows the SEM images of CNF group samples obtained from sample C-TiO₂ by hydrothermal treatment using the different conditions, as Fig. 1. All samples maintained the previous nanoparticle morphology, indicating that the hydrothermal treatment with concentrated NaOH was not able to obtain titanate. Only the samples CNF-III and CNF-IV showed some minimum formation of fibers. Possibly, the treatment at higher temperatures (150 °C) is

more capable to dissolve and rearrange TiO₂ nanoparticles, producing titanate fibers.

As mentioned before, C-TiO₂ nanoparticles consist of anatase and rutile phases. This rutile phase can be isolated or attached to anatase phase. In some cases, anatase can be covered by rutile, forming a thin layer [31, 32]. As showed by Fig. 2, C-TiO₂ had higher nanoparticles sizes than H-TiO₂ nanoparticles, decreasing the surface area and, consequently, the region of interaction with the NaOH solution. In this way, to dissolve and rearrange rutile nanocrystals into titanate nanorods, higher temperatures and/or more concentrated NaOH solution would be necessary [37].

Figure 7a-d shows the SEM images of HNF group samples, obtained from hydrothermal process of sample

Fig. 6 SEM images of samples **a** CNF-I, **b** CNF-II, **c** CNF-III, and **d** CNF-IV

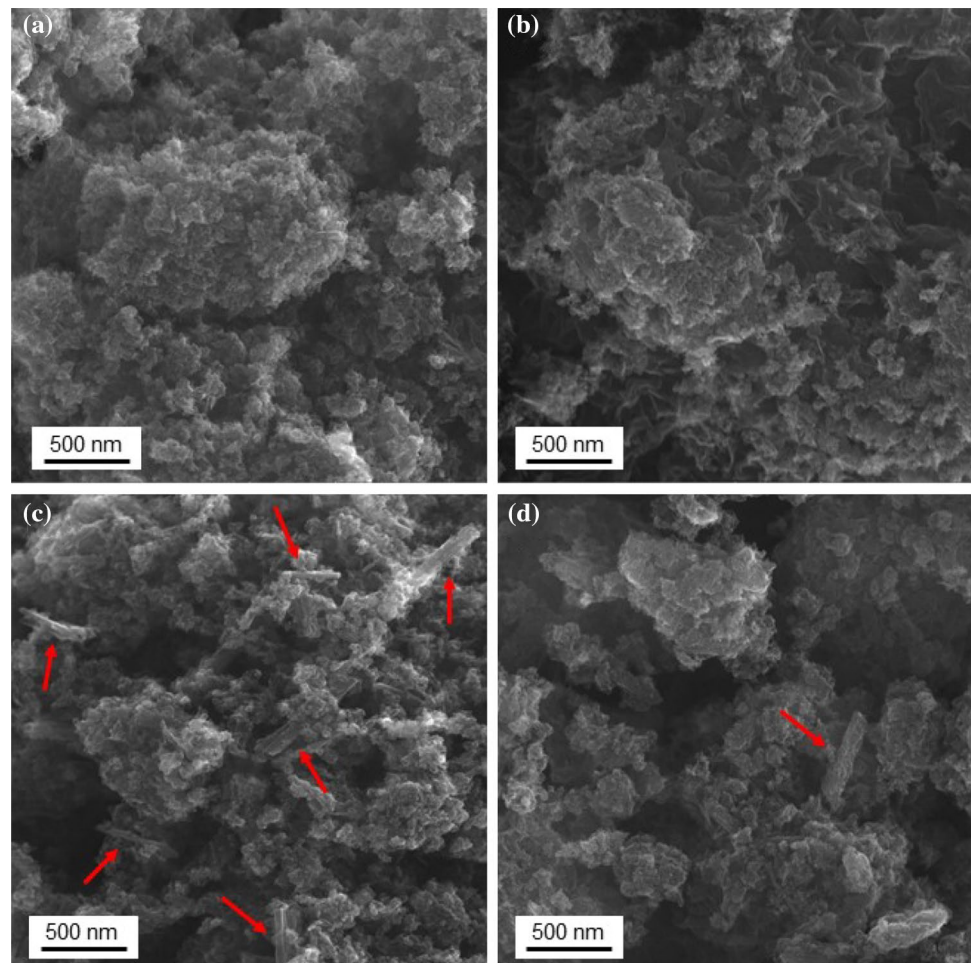
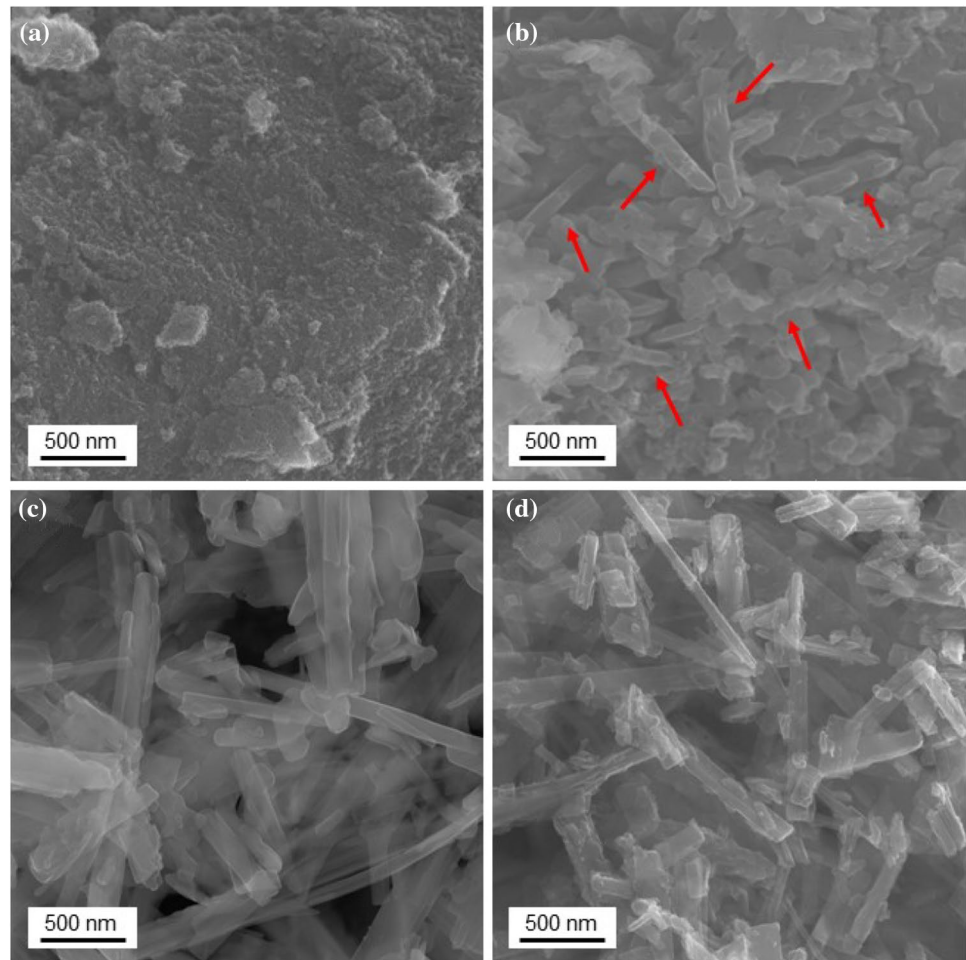


Fig. 7 SEM images of samples **a** HNF-I, **b** HNF-II, **c** HNF-III, and **d** HNF-IV



H-TiO₂, according to Fig. 1. In contrast to CNF samples, HNF presented the formation of nanorods in some conditions. Only the sample HNF-I (Fig. 7a) did not suffer any morphological modification after the NaOH hydrothermal treatment. Probably, the set parameter of time (24 h) and temperature (100 °C) were not enough to perform the phase transition to titanate nanorods. The sample HNF-II, treated at 100 °C during 48 h (Fig. 7b) presented the formation of some nanorods. The presence of structures in a form of plates can also be observed, which can be related to titanate sheets that recrystallized, but did not have enough energy to fold in nanorods [17]. These resultant structures appear to be an intermediate phase of incomplete transition products. In this case, TiO₂ coexist with titanates, with different morphologies [37].

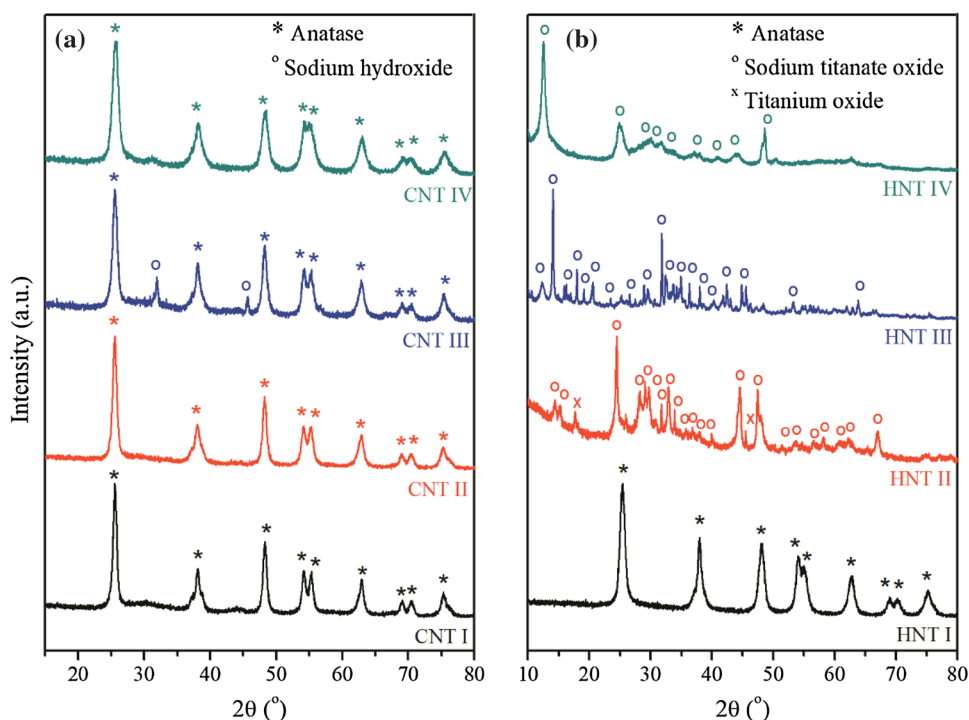
The samples HNF-III and HNF-IV (Fig. 7c-d) presented the best results. Both samples were treated at 150 °C and showed a significative number of nanorods. Although the nanorods are clustered, their sizes are regular and uniform. The diameter of the fibers was similar, being $\sim 119 \pm 30$ nm for the sample HNF-III and $\sim 111 \pm 36$ nm for sample HNF-IV. Sample HNF-III presented more regular and

homogeneous tubes, while the sample HNF-IV showed tubes with rough surfaces and heterogeneous length.

Figure 8a, b presents the XRD patterns of CNF (Fig. 8a) and HNF (Fig. 8b) samples. As expected, the samples of CNF group are not constituted of titanate structures. All samples (CNF-I, CNF-II, CNF-III, and CNF-IV) showed peaks indexed to the tetragonal phase of anatase (JCPDS 21-1272). The hydrothermal treatment of C-TiO₂ particles was not able to obtain titanate fibers, it only to rearrange the rutile/anatase phases to pure anatase. Only the sample CNF-III presented two peaks around 32° and 45° related to the sodium titanate phase of nanorods formation (JCPDS 35-1009). As mentioned before, the presence of rutile phase on C-TiO₂ along with the higher particle size may difficult the transformation of TiO₂ into titanate nanorods.

Figure 8b showed the XRD profiles of HNF group samples. HNF-I is formed by tetragonal anatase phase (JCPDS 21-1272). The low synthesis temperature (100 °C) and time (24 h) used in HNF-I synthesis was not high enough for the formation of titanate tubes. The sample HNF-II presented the formation sodium titanate Na₂Ti₂Ti₆O₁₆ (JCPDS 19-1249) and monoclinic TiO₂

Fig. 8 XRD patterns nanorods powders of samples CNF (a) and HNF(b)



(JCPDS 03-065-1156). Although a longer reaction time was used (48 h), probably the low temperature (100 °C) was not high enough to transform all TiO₂ into titanates. Therefore, HNF-II is an intermediate phase related to incomplete transition reaction.

XRD patterns of HNF-III showed the presence of sodium titanate oxide as Na₄Ti₅O₁₂ (JCPDS 01-075-2497) and Na₂Ti₉O₁₉ (JCPDS 33-1293). Sample HNF-IV showed a layered hydrogen titanate structure as H₂Ti₃O₇·xH₂O (JCPDS 47-0561) with monoclinic lattice [37, 38]. Samples HNF-III and HNF-IV presented fibril morphologies with different phases, indicating that higher hydrothermal treatment temperatures (150 °C) lead to tube formation. Therefore, the hydrothermal temperature has a significant effect on the morphology and structure of the resulting sample. The nucleation and crystal growth of the nanorods are directly influence by temperature [39]. Besides, the use of anatase as precursor strongly influenced in the nanorods production. Anatase has a tendency for continuous growth in a specific direction during the reaction with NaOH solution, being more effective than a mixture of anatase/rutile phases [39]. As mentioned before, the TiO₂ nanoparticles of H-TiO₂ sample are formed by highly pure anatase with particle size under 15 nm. For this reason, the formation of titanate nanorods was more favorable for H-TiO₂ than for commercial TiO₂ samples (C-TiO₂), which had a fraction of rutile along with anatase.

3.3 Photodegradation

The UV-Vis spectra of nanoparticles suspension after stirring in the presence of MB showed increased absorbance at 610 nm which corresponds to the dimer absorption band. This effect was already expected since the dimerization of MB under adsorption on negatively charged surfaces was reported before [40, 41]. Even so, the absorption band at 660 nm was used in order to monitor the MB degradation and the absorption band at 292 nm was used to monitor nanoparticles photo stability. The photodegradation efficiency after 30 min of irradiation in each

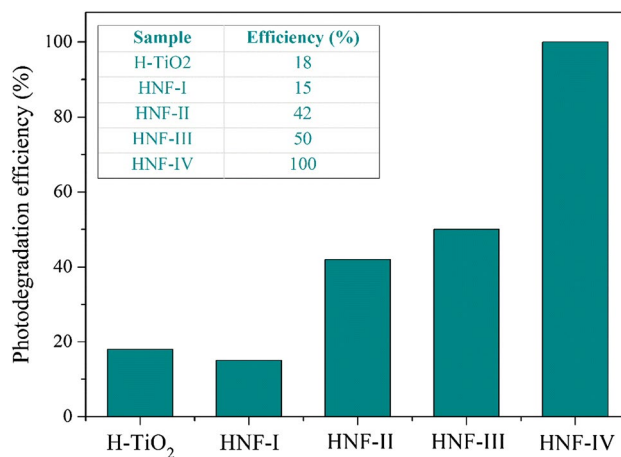


Fig. 9 Values of photodegradation efficiency of MB (15µM) after 30 min of UV-irradiation

nanoparticle suspensions is depicted in Fig. 9. The absence of MB absorption band after 30 min of UV irradiation of HNF-IV showed the higher activity of these nanoparticles in comparison with the others. Notably, the photodegradation efficiency increased with the increase of titanates nanorods content in the sample. This result was in line with the observations of Zhang et al. [42]. In their work, the authors showed enhanced photocatalytic activity in function of the increased aspect ratio of ZnO nanorods.

Since the photodegradation of MB by HNF-IV nanoparticles was too fast, the MB concentration was doubled, and the photodegradation was monitored with shorter time intervals. Figure 10 shows the UV-Vis absorption spectra of HNF-IV nanoparticles before and after different times of irradiation. It was possible to note the decrease of MB

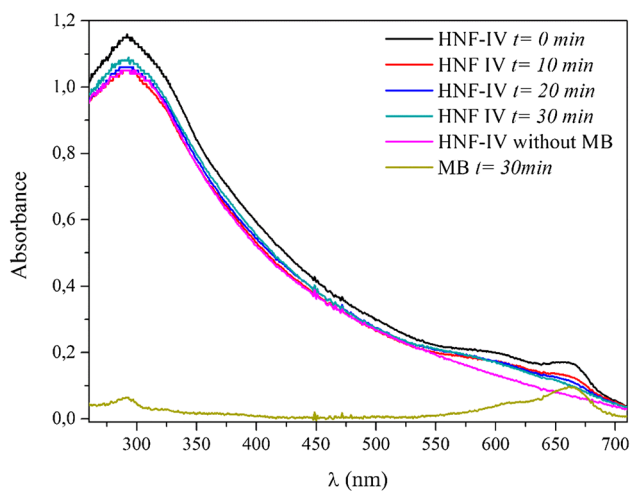


Fig. 10 UV-Vis absorption spectra of HNF-IV nanoparticles in the absence and presence of MB after different times of irradiation

absorption in function of time while absorbance of TiO_2 (292 nm) was constant. These results suggested that the HNF-IV presented high photo stability.

The values of photodegradation efficiency in function of time for HNF-IV are depicted in Fig. 11. The kinetic curve showed a fast degradation rate and even if MB concentration was of 30 μM , more than 70% of MB was degraded after only 30 min of UV irradiation. For comparative purpose, similar assay was performed with HNF-III. In this case, MB concentration was lower (15 μM) and the degradation of MB was monitored until 120 min. Figure 11 showed a fast kinetic of degradation but the nanoparticles were able to degrade 100% of MB only after 120 min. Therefore, it was evident the influence of the nanorods content in the photo catalytic activity of titanates. Even if both HNF-III and HNF-IV were composed of titanates nanorods, the presence of nanoparticles with different morphologies and lower nanorods content in the HNF-III samples was enough to compromise their photodegradation efficiency.

It is important to mention that no changes on the MB UV-Vis spectra was observed after 120 min of irradiation in the absence of nanoparticles nor in the UV-Vis spectra of MB in the presence of nanoparticles kept 120 min in the dark. These observations confirmed that the degradation of MB was a result of the photo activity of TiO_2 nanoparticles under UV irradiation.

4 Conclusion

TEM and XRD results of TiO_2 nanoparticles showed that the particle size and average crystallite size are correlated with the phases observed in the samples. According to the literature, rutile structure is more stable under

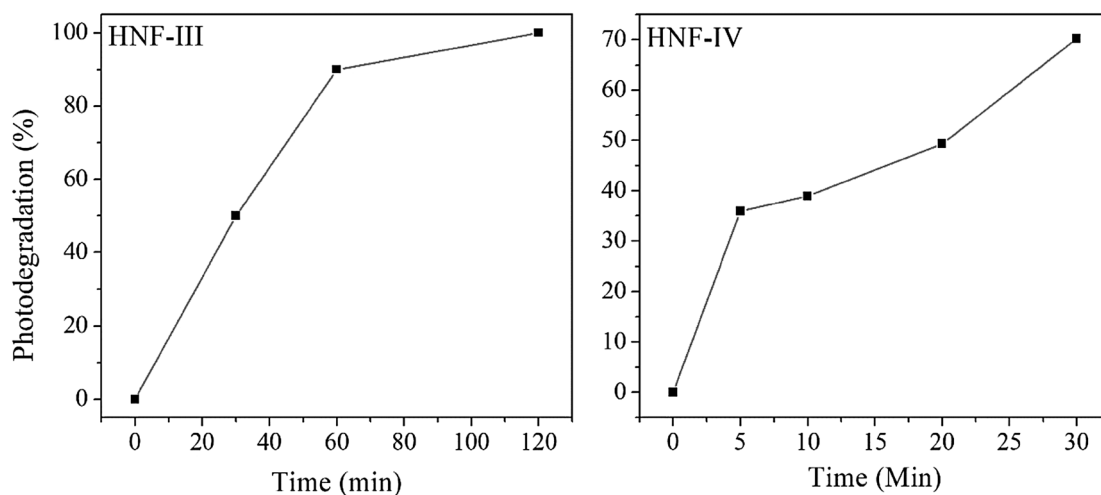


Fig. 11 Photodegradation efficiency (%) of HNF-III and HNF-IV in function of irradiation time. [MB]=30 μM in the HNF-IV suspension and [MB]=15 μM in the HNF-III suspension

ambient conditions, while anatase phase is more stable in nanometer size under 15 nm. For hydrothermally synthesized TiO₂ (H-TiO₂), only anatase phase was obtained with particle size of about 10 nm. On the other hand, for commercial TiO₂ samples (C-TiO₂), a fraction of rutile was observed, and the particles presented size above 15 nm (~ 20 nm). The crystalline structure of the precursor had a significant effect on the final product of the hydrothermal reaction. According to the results, the presence of rutile on TiO₂ nanoparticles hinders the phase transition into titanates. Rutile is the most thermodynamically stable phase of TiO₂, presenting the higher chemical stability. In this way, higher temperature or more concentrated NaOH solution should be necessary to obtain titanates using a mixture of anatase and rutile as precursor. On the other hand, by using pure anatase as precursor, different results were obtained. As showed by SEM micrographs, the phase transition into titanate nanorods occurred at higher temperatures (150 °C) regardless of reaction time. XRD patterns showed the formation of sodium titanates for samples HNF-II and HNF-III and hydrogen titanates for the sample HNF-IV, indicating that the time of reaction defined its crystal structure. Photodegradation tests showed that photodegradation efficiency is higher for titanates nanorods when compared to TiO₂ nanoparticles. This study showed that hydrothermal reaction was able to produce titanate nanorods, and that the synthesis parameters are extremely important in the final structure, morphology, and application.

Acknowledgements The authors acknowledge Coordenação de Aperfeiçoamento de Pessoa de Nível Superior (CAPES), Conselho Nacional de Desenvolvimento Científico e Tecnológico (CNPq), and Fundação de Amparo à Pesquisa do Estado de São Paulo (FAPESP, Grant 2017/02846-5, 2017/01697-6, 2017/24873-4, 2018/12035-7, and 2019/00568-3) for financial support.

Compliance with ethical standards

Conflict of interest The authors declare that they have no conflict of interest.

References

1. Carp O, Huisman CL, Reller A (2004) Photoinduced reactivity of titanium dioxide. *Prog Solid State Chem* 32:33–177
2. Govindaraj R, Santhosh N, Pandian MS, Ramasamy P, Sumita M (2018) Fabrication of stable dye-sensitized solar cell with hydrothermally synthesized titanium dioxide nanorods as a photoanode material. *J Mater Sci Mater Electron* 29:3736–3743
3. Mbonyiriyivuze A, Zongo S, Diallo A, Bertrand S, Minani E, Yadav LL, Mwakikunga B, Dhlamini SM, Maaza M (2015) Titanium dioxide nanoparticles biosynthesis for dye sensitized solar cells application: review. *Phys Mater Chem* 3:12–17
4. Taziwa R, Meyer EL, Sideras-Haddad E, Erasmus RM, Manikandran E, Mwakikunga BW (2012) Effect of carbon modification on the electrical, structural, and optical properties of TiO₂ electrodes and their performance in lab-scale dye-sensitized solar cells. *Int J Photoenergy* 904323:9
5. Sikhwivhilu LM, Mpelane S, Mwakikunga BW, Ray SS (2012) Photoluminescence and hydrogen gas-sensing properties of titanium dioxide nanostructures synthesized by hydrothermal treatments. *Appl Mater Interfaces* 4:1656–1665
6. Lu P, Fang S, Cheng W, Huang S, Huang M, Cheng H (2018) Characterization of titanium dioxide and zinc oxide nanoparticles in sunscreen powder by comparing different measurement methods. *J Food Drug Anal* 26:1192–12000
7. Gold K, Slay B, Knackstedt M, Gaharwar AK (2018) Antimicrobial activity of metal and metal-oxide based nanoparticles. *Adv Ther*. <https://doi.org/10.1002/adtp.201700033>
8. Ruiz PA et al (2017) Titanium dioxide nanoparticles exacerbate DSS-induced colitis: role of the NLRP3 inflammasome. *Gut* 66:1216–1224
9. Bozzi A, Yuranova T, Guasaquillo I, Laub D, Kiwi J (2005) Self-cleaning of modified cotton textiles by TiO₂ at low temperatures under daylight irradiation. *J Photochem Photobiol A* 174:156–164
10. Braun JH, Baidins A, Marganski RE (1992) TiO₂ pigment technology: a review. *Prog Org Coat* 20:105–138
11. Kettunen M et al (2011) Photoswitchable superabsorbency based on nanocellulose aerogels. *Adv Funct Mater* 21:510–517
12. Braga NF et al (2018) PHBV-TiO₂ mats prepared by electrospinning technique: physico-chemical properties and cytocompatibility. *Biopolymers* 109:e23120
13. Li Y, Bian Y, Qin H, Zhang Y, Bian Z (2017) Photocatalytic reduction behavior of hexavalent chromium on hydroxyl modified titanium dioxide. *Appl Catal B* 206:293–299
14. Chen X, Mao SS (2007) Titanium dioxide nanomaterials: synthesis, properties, modifications, and applications. *Chem Rev* 107:2891–2959
15. Gupta S, Tripathi M (2012) A review on the synthesis of TiO₂ nanoparticles by solution route. *Open Chem* 10:279–294
16. Yu J, Wang G, Cheng B, Zhou M (2007) Effects of hydrothermal temperature and time on the photocatalytic activity and microstructures of bimodal mesoporous TiO₂ powders. *Appl Catal B* 69:171–180
17. Zhang S, Peng LM, Chen Q, Du GH, Dawson G, Zhou WZ (2003) Formation mechanism of H₂Ti₃O₇ nanotubes. *Phys Rev Lett* 91:256103
18. Ma R, Fukuda K, Sasaki T, Osada M, Bando Y (2005) Structural features of titanate nanotubes/nanobelts revealed by Raman, X-ray absorption fine structure and electron diffraction characterizations. *J Phys Chem B* 109:6210–6214
19. Dumitriu C et al (2018) Production and characterization of cellulose acetate–titanium dioxide nanotubes membrane fraxiparinized through polydopamine for clinical applications. *Carbohydr Polym* 181:215–223
20. Meyerink J, Kota D, Wood S, Crawford G (2018) Transparent titanium dioxide nanotubes: processing, characterization, and application in establishing cellular response mechanisms. *Acta Biomater* 79:364–374
21. Ramos-Tonello CM et al (2017) Titanium dioxide nanotubes addition to self-adhesive resin cement: effect on physical and biological properties. *Dent Mater* 33:866–875
22. Abdullah M, Kamarudin S (2017) Titanium dioxide nanotubes (TNT) in energy and environmental applications: an overview. *Renew Sust Energy Rev* 76:212–225
23. Grimes CA (2007) Synthesis and application of highly ordered arrays of TiO₂ nanotubes. *J Mater Chem* 17:1451–1457
24. Cerri I, Roussel J (2018) Vertically aligned titanium oxide nanotubes for fuel cell electrodes. U.S. Patent Application n. 10/090,531, 2 out. 2018

25. Habisreutinger SN, Leijtens T, Eperon GE, Stranks SD, Nicholas RJ, Snaith HJ (2014) Carbon nanotube/polymer composites as a highly stable hole collection layer in perovskite solar cells. *Nano Lett* 14:5561–5568
26. Zhou M, Glushenkov AM, Kartachova O, Li Y, Chen Y (2015) Titanium dioxide nanotube films for electrochemical supercapacitors: biocompatibility and operation in an electrolyte based on a physiological fluid. *J Electrochem Soc* 162:A5065–A5069
27. Bjursten LM, Rasmusson L, Oh S, Smith GC, Brammer KS, Jin S (2010) Titanium dioxide nanotubes enhance bone bonding in vivo. *J Biomed Mater Res A* 92:1218–1224
28. Kasuga T, Hiramatsu M, Hoson A, Sekino T, Niihara K (1998) Formation of titanium oxide nanotube. *Langmuir* 14:3160–3163
29. Rietveld H (1969) A profile refinement method for nuclear and magnetic structures. *J Appl Crystallogr* 2:65–71
30. Coelho A (2018) TOPAS and TOPAS-academic: an optimization program integrating computer algebra and crystallographic objects written in C++. *J Appl Crystallogr* 51:210–218
31. Jiang X et al (2018) Anatase and rutile in evonik aerioxide P25: Heterojunctioned or individual nanoparticles? *Catal Today* 300:12–17
32. Bickley RI, Gonzalez-Carreno T, Lees JS, Palmisano L, Tilley RJ (1991) A structural investigation of titanium dioxide photocatalysts. *J Solid State Chem* 92:178–190
33. Kibasomba PM, Dhlamini S, Maaza M, Liu C-P, Rashad MM, Rayan DA, Mwakikunga BW (2018) Strain and grain size of TiO₂ nanoparticles from TEM, Raman spectroscopy and XRD: the revisiting of the Williamson–Hall plot method. *Result Phys* 9:628–635
34. Allen NS, Mahdjoub N, Vishnyakov V, Kelly PJ, Kriek RJ (2018) The effect of crystalline phase (anatase, brookite and rutile) and size on the photocatalytic activity of calcined polymorphic titanium dioxide (TiO₂). *Polym Degrad Stabil* 150:31–36
35. Zhang W, He Y, Zhang M, Yin Z, Chen Q (2000) Raman scattering study on anatase TiO₂ nanocrystals. *J Phys D* 33:912
36. Swamy V, Kuznetsov A, Dubrovinsky LS, Caruso RA, Shchukin DG, Muddle BC (2005) Finite-size and pressure effects on the Raman spectrum of nanocrystalline anatase TiO₂. *Phys Rev B* 71:184302
37. Zhu HY, Lan Y, Gao XP, Ringer SP, Zheng ZF, Song DY, Zhao JC (2005) Phase transition between nanostructures of titanate and titanium dioxides via simple wet-chemical reactions. *J Am Chem Soc* 127:6730–6736
38. Chen Q, Du G, Zhang S, Peng LM (2002) The structure of trititanate nanotubes. *Acta Crystallogr B* 58:587–593
39. Lan Y et al (2005) Titanate nanotubes and nanorods prepared from rutile powder. *Adv Funct Mater* 15:1310–1318
40. Tada DB, Rossi LM, Leite CAP, Itri R, Baptista MS (2010) Nanoparticle platform to modulate reaction mechanism of phenothiazine photosensitizers. *J Nanosci Nanotechnol* 10:3100–3108
41. Severino D, Junqueira HC, Gugliotti M, Gabrielli DS, Baptista MS (2003) Influence of negatively charged interfaces on the ground and excited state properties of methylene blue. *Photochem Photobiol* 77:459–468
42. Zhang X, Qin J, Xue Y, Yu P, Zhang B, Wang L, Liu R (2014) Effect of aspect ratio and surface defects on the photocatalytic activity of ZnO nanorods. *Sci Rep* 4:4596

Publisher's Note Springer Nature remains neutral with regard to jurisdictional claims in published maps and institutional affiliations.